

Multi-fault classification of rotor systems based on phase feature of axis trajectory in noisy environments

Chunrong Hua^a, Libo Xiong^{a,*}, Lumei Lv^a, Dawei Dong^a, Huajiang Ouyang^b

^aSchool of Mechanical Engineering, Southwest Jiaotong University, Chengdu, Sichuan 610031, China

^bSchool of Engineering, University of Liverpool, Liverpool L69 3GH, UK

*Correspondence should be addressed to Libo Xiong; xionglibo2018@my.swjtu.edu.cn

ABSTRACT

As it is difficult to distinguish multiple rotor faults with similar dynamic phenomena in noisy environments, a multi-fault classification method is proposed by combining the extracted trajectory phase feature, a parameter-optimized variational mode decomposition (VMD) method and a light gradient boosting machine (LightGBM) model. The trajectory phase feature is extracted from an axis trajectory by fusing the frequency, amplitude and phase information related to rotor motion and can comprehensively describe the dynamic characteristics induced by different rotor faults. Firstly, the vibration displacement signals in two orthogonal directions are collected to construct the axis trajectories with twelve rotor states including healthy, unbalance, misalignment, single crack, multiple cracks and a mixture of them. Secondly, the trajectory phase feature is extracted from the vectorized axis trajectories, and the frequency spectra of trajectory phase angles under different rotor faults are analyzed through Fourier transform. Finally, a parameter-optimized VMD method combined with a LightGBM model is applied to classify multiple faults of rotor systems in different noisy environments based on the extracted trajectory phase feature. The twelve rotor states can be classified into nine categories based on the harmonic information of $1X-7X$ components (X is the rotating frequency of a rotor system) and other components with smaller amplitudes in the frequency spectra of trajectory phase angles. The average classification accuracy of the twelve rotor states exceeds 93.0% and the recognition rate for each kind of fault is greater than 77.5% in noisy environments. The simulated and experimental results demonstrate the effectiveness and adaptability of the proposed multi-fault classification method. This work can provide a reference for the condition monitoring and fault diagnosis of rotor systems in engineering.

Keywords: trajectory phase feature, axis trajectory, multi-fault classification, parameter-optimized VMD, coupled faults, noisy environments

1. Introduction

As the core component of rotating machinery, a rotor system determines the safety, stability and production efficiency of mechanical equipment. Due to manufacturing and installation errors and the effects of alternating loads, a rotor system is prone to diverse faults like unbalance, misalignment and cracks, which seriously threaten the operation reliability of rotating machinery. In addition, the coupling of multiple faults will further affect the operation stability of a rotor system and accelerate the failure of rotating machinery, eventually causing catastrophic accidents and huge maintenance costs. Therefore, it is of vital importance to perform condition monitoring and fault diagnosis on rotor systems to ensure the

healthy and stable operation of mechanical equipment [1].

Vibration-based methods have been commonly used in structural health monitoring and damage detection for the nondestructive, inexpensive, and expedient merits [2-4]. As one of the critical vibration responses of a rotor system, an axis trajectory of its shaft center is represented by vibration (displacement) signals in two perpendicular directions, which contains the amplitude and phase information of vibration responses in two orthogonal directions [5]. It also can comprehensively and visually reflect the motion status and the fault-induced changes in dynamic properties, serving an important role in dynamic analysis, condition monitoring and fault diagnosis of rotor systems [6].

A large number of investigations on axis trajectories have been carried out to study the dynamic phenomena of rotor systems with different faults. The dynamic influences of rub-impact on the trajectory shape and size of a rotor were studied during start-up and shutdown operating conditions [7, 8]. Li et al. [9, 10] analyzed the vibration responses of a mixed-flow pump under different rotor-stator interaction and flow rate condition based on axis trajectory plot, frequency spectrum and particle image velocimetry experiments. The nonlinear vibration behaviors of a rotor system under a coupling misalignment fault were investigated by analyzing the axis trajectory diagram, time waveform, frequency spectrum, and Poincare section diagram [11-13]. The dynamic responses of a cracked rotor are analyzed with the evolution of whirl orbit shape around $1/2$, $1/3$ and $1/4$ subcritical speeds [14-17]. Ma et al. [18] studied the steady-state responses of a reduced dual-rotor system with nonlinear bearings and squeeze film damper based on rotor orbits and spectrum cascades. Shi et al. [19] found that the ring squeeze film damper can regulate the rotor vibration significantly, and help the rotor shaft trajectory quickly converge to a balanced state. Varney and Green [20] analyzed the influence of support asymmetry degree on the nonlinear vibration responses of rotor systems. Lin et al. [21] studied the dynamic characteristics of a rotor system with a loosened sliding bearing support under the same direction eccentricity and reverse eccentricity conditions. In addition, the study of coupling dynamic behaviors under various faults has also received some attention. Gasch [22] used the two-sided spectral order analysis method to study the effects of crack and unbalance faults on the forward and backward whirl orbit shape and size for a Laval rotor. Li et al. [23, 24] adopted rotor orbits to study the effects of the bolted-disk joint stiffness and eccentric phase difference on the dynamic characteristics of a rotor-bearing system at different rotating speeds. Ma et al. [25-27] analyzed the dynamic characteristics of a rotor system under rubbing, eccentric phase differences between two discs, oil-film force and seal force through the trajectory amplitude and shape, vibration waveform.

Several scholars studied how to control or compensate rotor motion on the basis of the changes of the axis trajectories. Zhou et al. [28] proposed an adaptive unbalance compensation algorithm for a maglev rotor and verified its effectiveness by comparing the axis trajectory shape and size before and after compensation. Ahad et al. [29] used the orbit visualization plots to evaluate the control performance of a classical PID and modern state-space control strategies for the maglev rotor motion. Kalista et al. [30] adopted a general notch filter algorithm to control the trajectory shape of an active magnetic bearing (AMB) rotor system. Lahiri et al. [31] analyzed the axis trajectory plots of a rotor system under rub-impact fault and designed an improved annular bearing to mitigate the influence of rub-impact on the lateral motion.

The axis trajectory contains very important information for fault diagnosis of rotor systems. The full spectrum analysis [7, 32] and energy identification methods [33, 34] were adopted to extract the shape

characteristics of an axis trajectory to diagnose rub-impact faults for rotor systems. Some approaches based on orbit shape [11], nonlinear output frequency response functions [13] and average rotor centerline plots [35] were used to detect misalignment faults. Zhang et al. [36] identified a shallow crack in a rotor by combining vibration energy and whirl orbit. Xie et al. [5] diagnosed a rotor crack by studying the relationship between crack breathing effect and the transient characteristics of axis trajectory.

The axis trajectory can provide a basis for multi-fault classification of rotor systems. Sinha [37] combined orbit plots and higher order spectra to identify crack and misalignment faults in a shaft. Xiang et al. [6] identified the crack and rub-impact faults of a rotor-bearing system based on the morphological characteristics of axis trajectories near $1/3$ and $1/2$ subcritical speeds. The feature-frequency separation methods based on singular value decomposition were presented to identify misalignment and rub impact faults in a rotor [38, 39]. Liu et al. [40] classified the orbit responses induced by rub, bouncing and pendulum vibration of an AMB rotor system during touchdowns through the mathematical expectation and discrete Fourier transform. Yang and Tavner [41] adopted EMD and high-resolution spectrum to purify a transient shaft trajectory and distinguished rotor-to-stator rub and fluid excitation faults of a centrifugal compressor. A two-dimensional sample entropy algorithm was proposed to extract the axis trajectory features and classify normal, unbalance, impact and collision faults of an AMB rotor [42].

The above researches provide a foundation for fault diagnosis of rotor systems based on the dynamic properties of axis trajectories, which mainly focus on a single or multiple faults (such as crack, misalignment, unbalance, rub-impact and collision) with different orbit morphological characteristics, and consider the simultaneous presence of only two single faults (crack and rub). However, in actual engineering, there are situations where rotor systems may suffer from the coupled faults (i.e. simultaneous multi-type faults) of unbalance, misalignment and cracks, owing to manufacturing and installation errors and the effects of alternating loads of rotating machinery. The axis trajectories of a rotor system with diverse faults may have similar shape features. For example, the axis trajectory shapes of both healthy and unbalanced horizontal rotors are elliptical, the axis trajectories at $1/2$ subcritical speed under misalignment, crack and misalignment-crack faults all contain an inner loop. Moreover, the axis trajectories will be inevitably distorted as the practical collected vibration signals will be inevitably contaminated by ambient noise, resulting in a great difficulty in the multi-fault classification of rotor systems.

The occurrence of multiple faults, the similarity of the morphological characteristics of the axis trajectory under multiple faults and the noise contamination will all increase the difficulty in fault identification of a rotor system based on axis trajectories. Focusing on these challenges, a multi-fault classification method combining the extracted trajectory phase feature, a parameter-optimized VMD method and a LightGBM model is proposed to distinguish twelve rotor states of different kinds (including healthy, three single faults and eight coupled faults) at nine signal-to-noise ratios (SNRs). Firstly, the vibration displacement signals of the shaft axis in two orthogonal directions are collected to synthesize the axis trajectories. Secondly, the trajectory phase feature is extracted by vectorizing the axis trajectories to characterize the fault-induced dynamic properties of a rotor system, and the frequency spectra of trajectory phase angles are analyzed through Fourier transform. Thirdly, a parameter-optimized VMD based on non-dominated sorting genetic algorithm-III (NSGA-III) is introduced to denoise the trajectory phase angles at different SNRs. Finally, the denoised trajectory phase angles are input into a

LightGBM model to identify the multiple faults of a rotor system.

The remainder is organized as follows. In Section 2, the extracted trajectory phase feature is detailed. A parameter-optimized VMD based on NSGA-III is introduced. The LightGBM model is reviewed and the general procedure of this method is shown. In Section 3, the dynamic responses of a rotor system model under various faults are analyzed, and the multi-fault classification results under different SNRs are given. The experimental validation is conducted and the results are discussed in Section 4. Finally, the conclusions are summarized in Section 5.

2. Basic principle

Focusing on the difficulty in distinguishing multiple rotor faults with similar dynamic behaviors in noisy environments, a multi-fault classification method is proposed by combining the extracted trajectory phase feature, a parameter-optimized VMD method and a LightGBM model in this section.

The trajectory phase feature is extracted from an vectorized axis trajectory by integrating the frequency, amplitude and phase information related to rotor motion, which is utilized to characterize the rotor motion under different kinds of states (including healthy, unbalance, misalignment, single crack, multiple cracks, unbalance-misalignment, unbalance-single crack, unbalance-multiple cracks, misalignment-single crack, misalignment-multiple cracks, unbalance-misalignment-single crack, unbalance-misalignment-multiple cracks).

A parameter-optimized VMD based on NSGA-III is presented to decompose and denoise the trajectory phase angles at different SNRs (20, 15, 10, 5, 0, -5, -10, -15, -20 dB). The improved VMD method can guarantee the signal decomposition accuracy and denoising performance in different noisy environments with less time loss over the traditional one.

The LightGBM model has the advantages of high fitting speed, high accuracy, low memory consumption and supporting parallel data processing, which is thereby employed to identify multiple faults of a rotor system in this study. And the denoised trajectory phase angles are randomly divided into training samples and testing samples for LightGBM with a ratio of 7:3.

For the sake of brevity, all data used in the proposed method are under the coupled fault of unbalance-misalignment-multiple cracks, unless otherwise specified. And letters A-L are used to denote the above twelve rotor states in the following text.

2.1 Trajectory phase feature

For a cracked rotor system (shown in Fig. 1), the vibration displacement signals in the Y and Z directions can be expressed as [43]:

$$\begin{cases} y_i(t) = A_i \sin(2\pi f_i t + \varphi_i) \\ z_i(t) = B_i \sin(2\pi f_i t + \psi_i) \end{cases} \quad (1)$$

where t is the sampling time; i represents different frequency components, $i = 1, 2, 3, \dots$; A_i , B_i are the amplitudes of the i -th order frequency component in the Y and Z directions, respectively; φ_i , ψ_i are the initial time phases; f_i is the frequency of the i -th order component.

The vibration displacement signals in the Y and Z directions are usually analyzed separately by Fourier transform, shown in Figs. 2(a)-(b). As a result, the phase correlation between the motion in two

directions of the same rotation plane are ignored, resulting in incomplete feature extraction and incorrect fault diagnosis results [32]. To unify the simulated and experimental coordinate systems below, all axis trajectories are generated by the vibration displacement signals in both Y and Z directions.

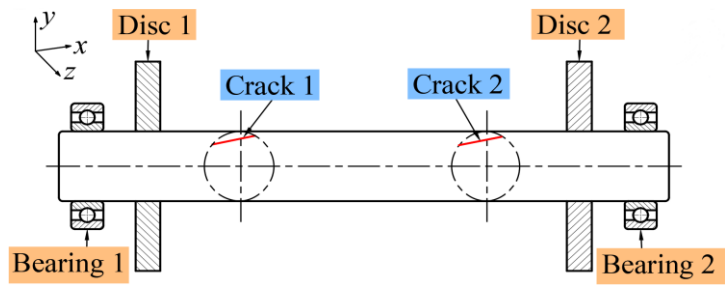


Fig. 1. Model of cracked rotor system.

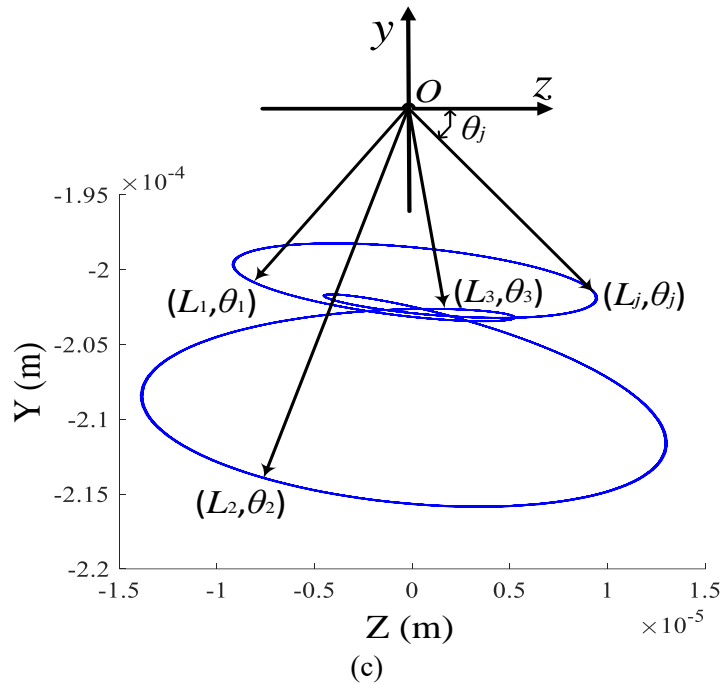
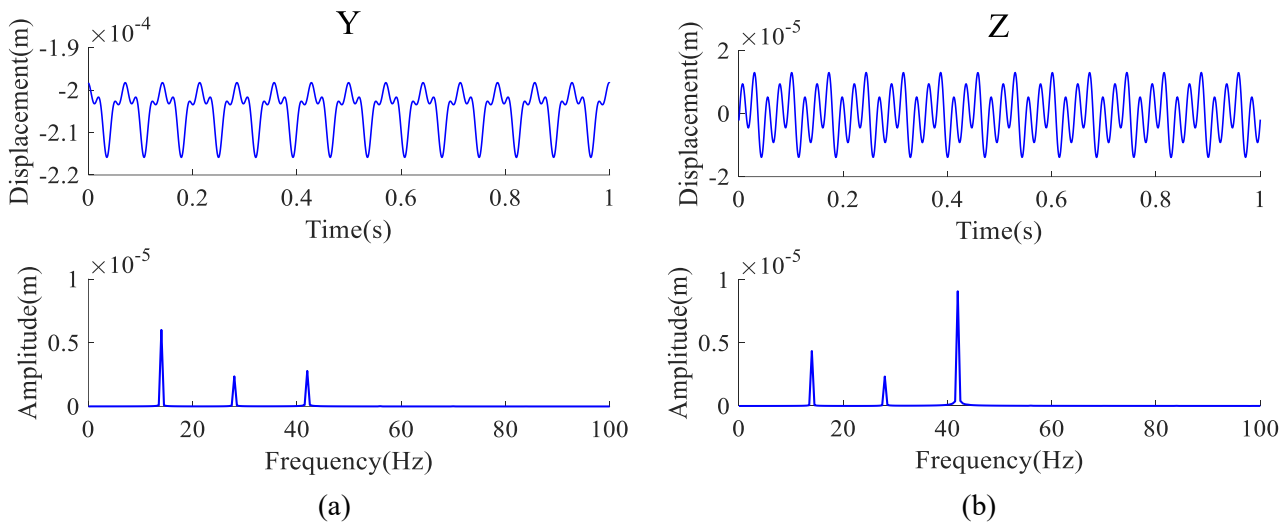


Fig. 2. Vibration responses of rotor system under unbalance-misalignment-multiple cracks, (a) Displacement signal in Y direction, (b) Displacement signal in Z direction, (c) Trajectory vectors.

An axis trajectory (shown in Fig. 2(c)) contains the amplitude and phase information of vibration responses in two orthogonal directions, and has a significant value for fault diagnosis of rotor systems [5]. However, in some special cases, rotor systems under different kinds of faults have similar axis trajectories, which will lead to misdiagnosis of rotor faults. For instance, the axis trajectory shapes of a healthy and an unbalanced horizontal rotor systems are elliptical, while those at 1/2 subcritical speed under misalignment, crack and misalignment-crack faults contain an inner loop. Therefore, further feature extraction of axis trajectories is essential to provide comprehensive discrimination information to accurately identify different kinds of faults of rotor systems.

Inspired by the full spectrum method that fuses the frequency, amplitude and phase information of vibration signals in two perpendicular directions [43, 44], an axis trajectory is vectorized to extract adequate and valuable information on rotor motion. In the global YOZ coordinate plane, a series of trajectory vectors can be obtained by connecting the static coordinate origin to any point on the axis trajectory, shown in Fig. 2(c). Any trajectory vector \mathbf{L}_j can be expressed as:

$$\mathbf{L}_j = \mathbf{Y}_j + \mathbf{Z}_j \quad (2)$$

where \mathbf{Y}_j and \mathbf{Z}_j are the vibration displacement vectors in the Y and Z directions, respectively. $j = 1, 2, 3, \dots, V$; V is the number of data points on the axis trajectory.

And the length L_j and phase θ_j of any trajectory vector can be derived as:

$$L_j = |\mathbf{L}_j| = \sqrt{|\mathbf{Y}_j|^2 + |\mathbf{Z}_j|^2} \quad (3)$$

$$\theta_j = \langle \mathbf{L}_j, \mathbf{Z}_j \rangle = \arccos \left(\frac{\mathbf{L}_j \cdot \mathbf{Z}_j}{|\mathbf{L}_j| \cdot |\mathbf{Z}_j|} \right) \quad (4)$$

where $|\cdot|$ represents the Euclidean norm of a set.

The extracted trajectory length and phase angle are depicted in Fig. 3. The values of trajectory length in Fig. 3(a) are always non-negative, missing the quadrant of the axis trajectory in both coordinates, so cannot be applied to classify the multiple faults of a rotor system.

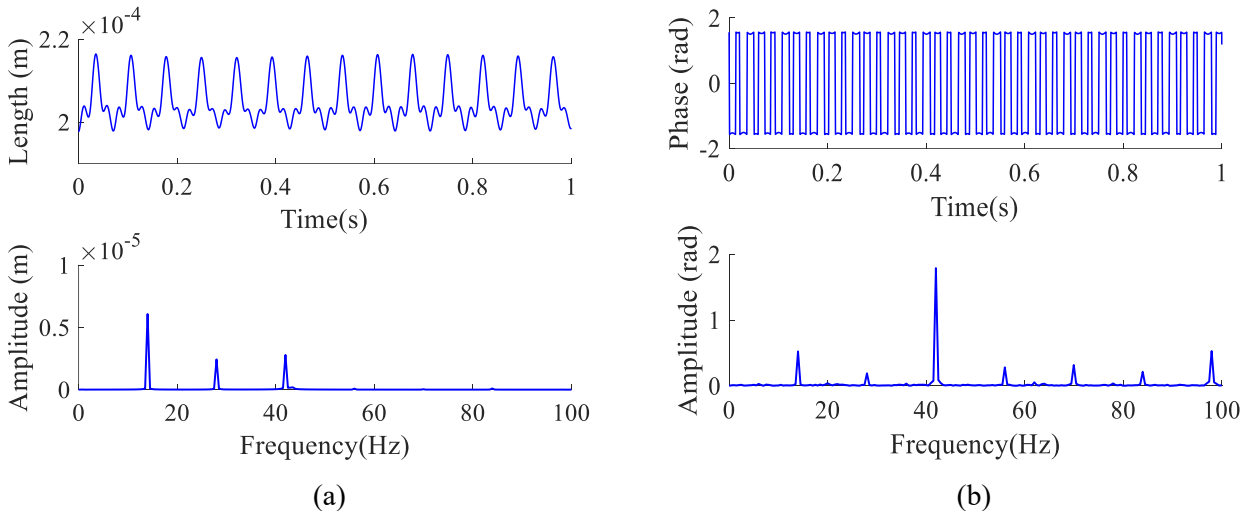


Fig. 3. Extracted trajectory vector features under unbalance-misalignment-multiple cracks, (a) Length, (b) Phase angle.

The phase feature of the axis trajectory integrates the frequency, amplitude and phase information of rotor motion in the Y and Z directions simultaneously. The extraction of trajectory phase feature needs a smaller computational effort than the full spectrum method as the axis trajectory does not need to be

decomposed into a series of forward and backward whirl-filtered trajectories with different frequencies. It can be seen from Fig. 3(b) that the waveform of the trajectory phase angle in time domain approximates a rectangular wave. And there are more higher-order harmonic components in the frequency spectrum that are very sensitive to changes in structural stiffness, besides the first three harmonic components. Hence, the trajectory phase feature extracted from the axis trajectory can provide more comprehensive information of rotor motion, which can be utilized to characterize the dynamic properties of rotor systems with different kinds of faults.

2.2 Parameter-optimized VMD

VMD [45] is an adaptive and non-recursive signal decomposition method for non-stationary and nonlinear signals, which assumes that any signal is composed of a series of intrinsic mode functions (IMFs) each with a specific center frequency and a limited bandwidth. According to [46, 47], the mode number K and quadratic penalty term α have great influences on decomposition results. Accordingly, seeking the optimal parameter combination (K - α) is the core of the application of VMD, and is also one of the objectives of this work.

NSGA-III [48, 49] is an evolutionary multi-objective optimization genetic algorithm based on reference points, which can ensure the diversity of population members via adaptively updating a number of well-spread reference points.

In order to meet the above demands, a parameter-optimized VMD based on NSGA-III is presented to guarantee the signal decomposition accuracy and denoising performance in different noisy environments. The NSGA-III algorithm is improved to seek the optimal parameter combination (K - α) for the traditional VMD.

Here, the optimal value problem of the mode number K and the quadratic penalty term α is transformed into a multi-objective optimization problem in NSGA-III, described as:

find $x = \{K, \alpha\}$ to satisfy the following objective functions

$$\begin{aligned} & \min \sum_{k=1}^K \text{SampEn}(\text{IMF}_k) \\ & \omega_k = \frac{\int_0^\infty \omega |\hat{u}_k(\omega)|^2 d\omega}{\int_0^\infty |\hat{u}_k(\omega)|^2 d\omega} \quad \text{s.t.} \quad \begin{cases} 40\text{Hz} < \omega_2 < 44\text{Hz} \\ \min_{k \neq h} |\omega_k - \omega_h| > 25\text{Hz} \end{cases} \end{aligned} \quad (5)$$

with

$$K \in [8, 20], \alpha \in [1000, 4000]$$

where IMF_k denotes the k -th IMF $u_k(t)$ obtained by VMD, ω_k is the center frequency of IMF_k , $\hat{u}_k(\omega)$ is the Fourier transform of $u_k(t)$; $\text{SampEn}(\text{IMF}_k)$ is the sample entropy of IMF_k [42, 50]; ω_2 is the center frequency of IMF_2 (i.e. the natural frequency of a rotor system); $\omega_k - \omega_h$ is the central frequency difference between any two IMFs; and $1 < k, h < K$.

The parameters K and α of the population members are mostly decimal numbers in the iterative process of NSGA-III [51], reducing the convergence rate of the objective functions and increasing the optimization cost, which even causes the results of signal decomposition to be inaccurate. Aiming at solving the issues, the traditional NSGA-III algorithm is improved by preprocessing population members before member selection in every iterative step, as follows:

(1) Preprocessing of the mode number K

$$K_p^* = \text{Round}(K_p) \quad (6)$$

(2) Preprocessing of the quadratic penalty term α

$$\alpha_p^* = \text{Round}(\alpha_p) \quad (7)$$

where K_p and α_p are the parameters of VMD at the p -th generation before preprocessing, K_p^* and α_p^* are the parameters obtained by preprocessing K_p and α_p , and Round denotes the rounding function [51]. There are a series of Pareto optimal solutions in the F1 front, and the one that satisfies the box constraints and has the minimum sample entropy is selected as the optimal parameter combination (K - α) of VMD.

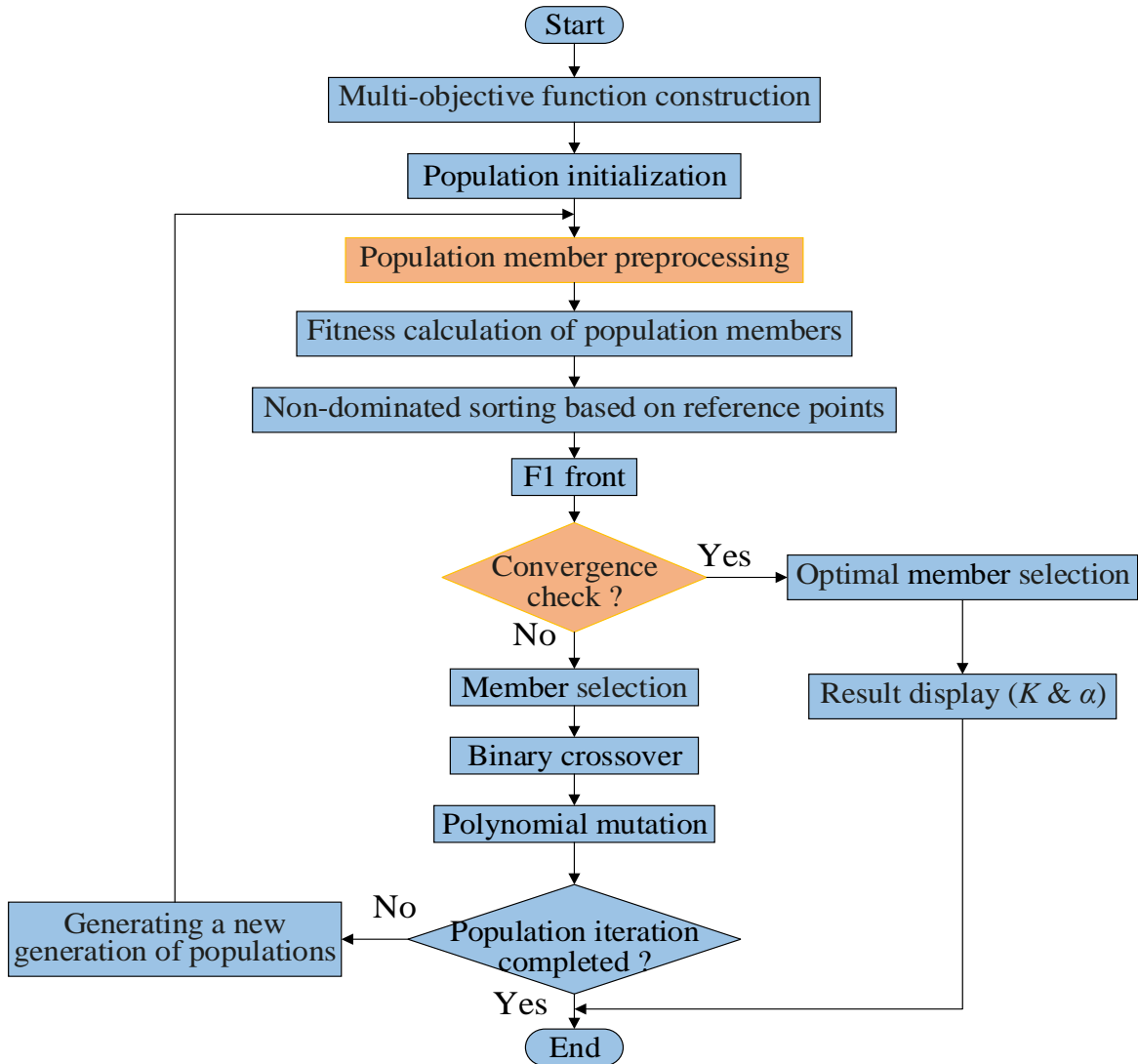


Fig. 4. Flowchart of VMD parameter optimization.

Moreover, in the conventional NSGA-III algorithm, it is only necessary to determine whether the members in the F1 front of the final generation satisfy the convergence conditions after all iterations are completed. In this process, the total optimization time consumption T_s can be expressed as

$$T_s = \sum_{p=1}^N t_p \quad (8)$$

where t_p is the time consumption at the p -th generation, and N is the preset population iteration number.

In order to facilitate optimization efficiency and reduce time consumption, several measures are taken to modify the flow of the conventional NSGA-III algorithm. The modified algorithm needs to judge whether the members in the F1 front of each generation meet the convergence conditions. And the iteration is terminated once a member satisfies the criteria. The total time consumption after modification is described as

$$T_s^* = \sum_{p=1}^{N^*} t_p \quad (9)$$

where N^* is the actual number of population iteration, $N^* \leq N$. The flowchart of the VMD parameter optimization based on NSGA-III is depicted in Fig. 4, and two modified parts are displayed with an orange background.

2.3 LightGBM

LightGBM [52] is an improved gradient boosting decision tree framework optimized by gradient-based one-side sampling, exclusive feature bundling, histogram algorithm and leaf-wise growth strategy with depth limitation. Its main idea is to update the model through continuous iterative training of decision trees. LightGBM has a good performance in pattern classification, which has been successfully applied to fault diagnosis in engineering [53, 54]. So a LightGBM model is used to identify the twelve rotor states in this work.

2.4 General procedure of the proposed method

As it is difficult to accurately distinguish different rotor faults with similar dynamic phenomena, a multi-fault classification method combining the extracted trajectory phase feature, a parameter-optimized VMD method and a LightGBM model is proposed to classify the twelve rotor states (including healthy, three single faults and eight coupled faults) in different noisy environments. This method mainly includes four steps, and the architecture is shown in Fig. 5.

Step 1. Collect the vibration displacement signals in the Y and Z directions to synthesize the axis trajectories of the rotor system with the twelve states.

Step 2. Vectorize the axis trajectories to extract the trajectory phase feature.

Step 3. Utilize a parameter-optimized VMD method to decompose and denoise the trajectory phase angles at different SNRs.

Step 4. The denoised trajectory phase angles are randomly divided into training samples and testing samples with a ratio of 7:3, which are then fed into a LightGBM model to classify diverse faults of rotor systems.

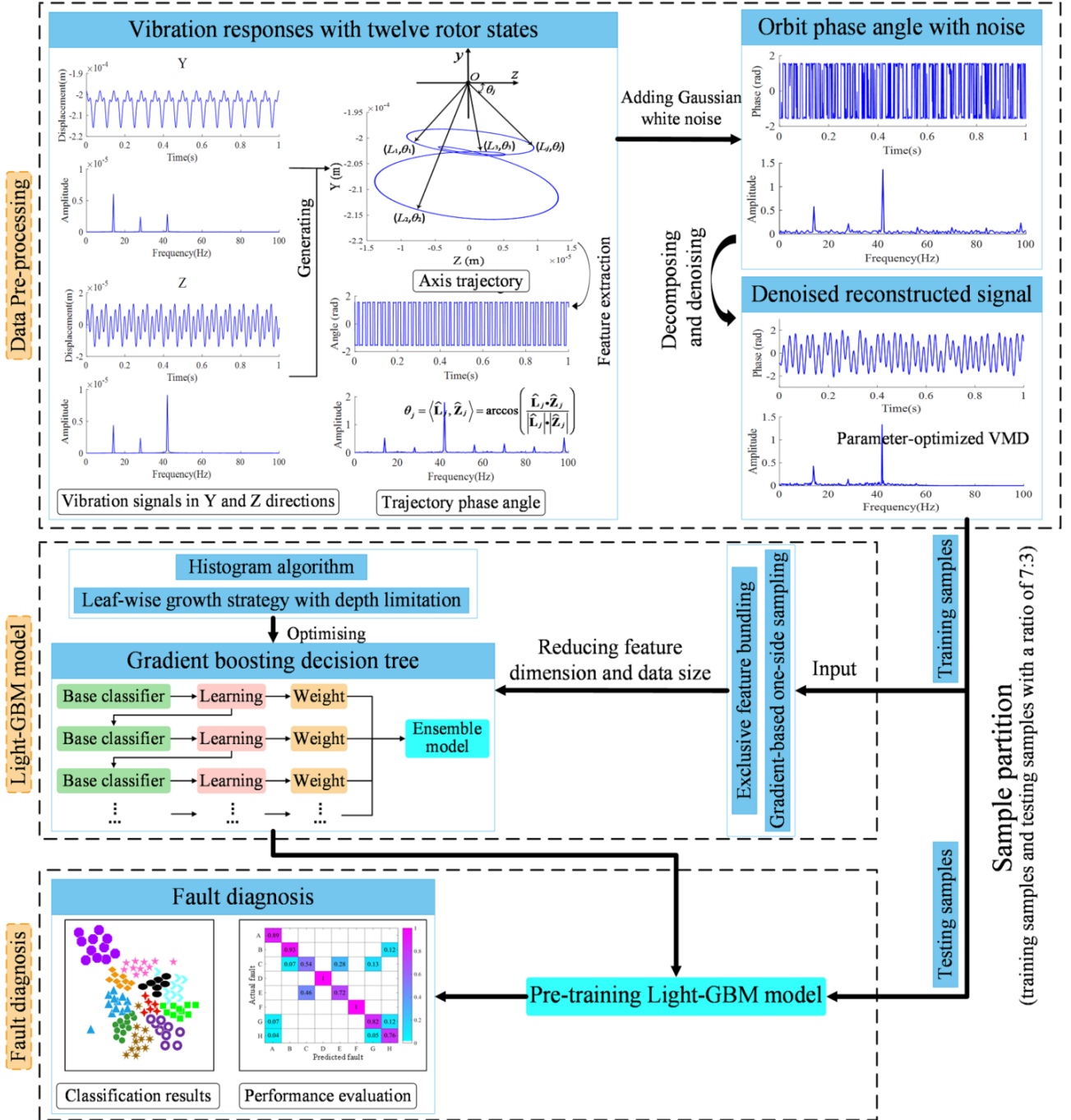


Fig. 5. Architecture of proposed method.

3. Multi-fault classification based on trajectory phase feature

The rotor system model [15, 55] consists of a shaft (discretized into 60 Timoshenko beam elements), two discs (regarded as rigid bodies) and two ball bearings (simplified as springs and dampers), as shown in Fig. 1. Some of the systemic physical parameters are given in Table 1. The first critical speed is calculated from the stiffness and mass of a healthy rotor system. The Rayleigh damping coefficients a and b are calculated by assuming that the first two modal damping ratios are 0.005 and 0.01, respectively.

Twelve rotor states are considered in this work including healthy, unbalance, misalignment, single

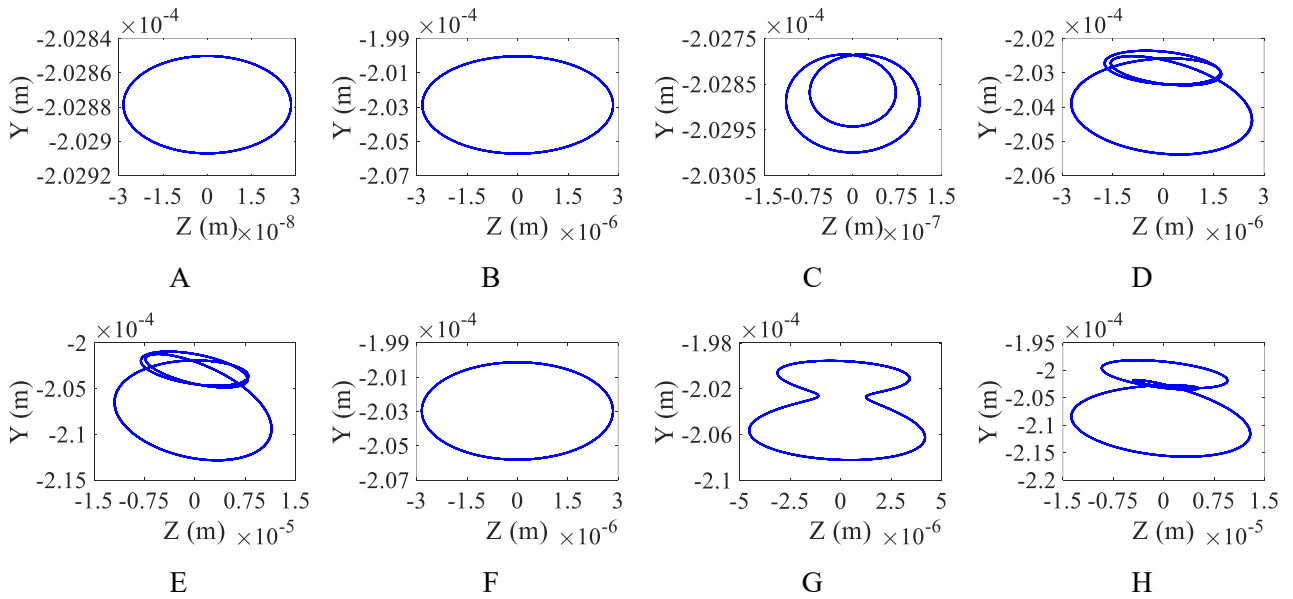
crack, multiple cracks, unbalance-misalignment, unbalance-single crack, unbalance-multiple cracks, misalignment-single crack, misalignment-multiple cracks, unbalance-misalignment-single crack, unbalance-misalignment-multiple cracks. The unbalance fault is produced by an eccentric mass on the two discs and the misalignment is obtained by biasing bearing 1. The single crack is located in the 30th element, while the parallel multiple cracks are in the 26th and 36th elements with a same depth of $0.2D$. The sampling point is located at the first disc with a sampling frequency of 1000 Hz, and the sampling time is 10 s.

Table 1. Physical parameters of rotor system.

Parameter	Value	Parameter	Value
Shaft diameter, D	0.01 m	Polar moment of inertia of disc 1	$5.76 \times 10^{-4} \text{ kg} \cdot \text{m}^2$
Shaft length	0.6 m	Diametrical moment of inertia of disc 1	$3.18 \times 10^{-4} \text{ kg} \cdot \text{m}^2$
Density of shaft (40Cr)	$7.87 \times 10^3 \text{ kg} \cdot \text{m}^{-3}$	Polar moment of inertia of disc 2	$5.84 \times 10^{-4} \text{ kg} \cdot \text{m}^2$
Disc eccentricity	$2.0 \times 10^{-5} \text{ m}$	Diametrical moment of inertia of disc 2	$3.23 \times 10^{-4} \text{ kg} \cdot \text{m}^2$
First critical speed, Ω_0	2520 rpm	Rayleigh damping coefficient, a	0.684
Mass of disc 1	0.759 kg	Rayleigh damping coefficient, b	2.80×10^{-5}
Mass of disc 2	0.770 kg		

3.1 Dynamic responses analysis

The occurrence of one or multiple faults will change the nonlinear stiffness and Rayleigh damping coefficients of a rotor system [55], which will aggravate the complexity of nonlinear vibration responses, resulting in more harmonic components in the frequency spectrum and more complex of the axis trajectory shape.



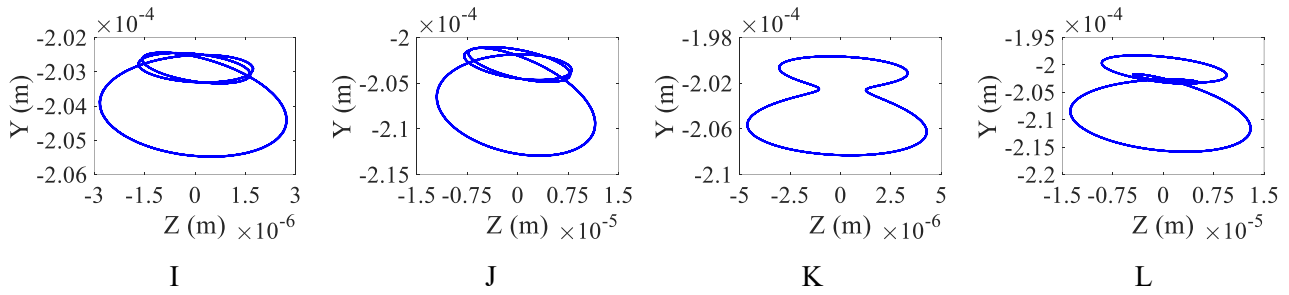
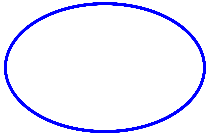
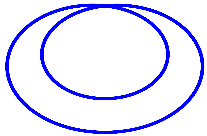
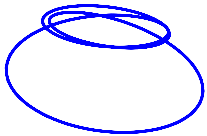
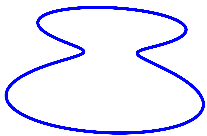



Fig. 6. Axis trajectories under different rotor states in noise-free environment, A: healthy, B: unbalance, C: misalignment, D: single crack, E: multiple cracks, F: unbalance-misalignment, G: unbalance-single crack, H: unbalance-multiple cracks, I: misalignment-single crack, J: misalignment-multiple cracks, K: unbalance-misalignment-single crack, L: unbalance-misalignment-multiple cracks.

The simulated axis trajectory plots of the rotor system with the twelve states in a noise-free environment are displayed in Fig. 6. Noting that the rotating speed of the shaft is set to 1/3 subcritical speed [14], i.e. 840 rpm, to highlight the crack feature in vibration responses of the rotor system. According to the morphological characteristics of the axis trajectories, the twelve rotor faults can be preliminarily categorized into five groups, shown in Table 2.

Table 2. Comparison of axis trajectories under twelve rotor states in noise-free environment.

Axis trajectory	Fault
	A: healthy B: unbalance F: unbalance-misalignment
	C: misalignment
	D: single crack E: multiple cracks I: misalignment-single crack J: misalignment-multiple cracks
	G: unbalance-single crack K: unbalance-misalignment-single crack
	H: unbalance-multiple cracks L: unbalance-misalignment-multiple cracks

It can be seen from Fig. 6 and Table 2 that the axis trajectories with healthy (A), unbalance (B), and

unbalance-misalignment (F) faults have the similar shape of an ellipse. The axis trajectory under misalignment (C) contains an inner loop. There are two inner loops on the top of the axis trajectories with a single crack (D), multiple cracks (E), misalignment-single crack (I) and misalignment-multiple cracks (J), while the trajectory size of the multi-crack rotor is larger than that of the single crack rotor. Both of the axis trajectories with unbalance-single crack (G) and unbalance-misalignment-single crack (K) contain two concaves. And the trajectories of unbalance-multiple cracks (H) and unbalance-misalignment-multiple cracks (L) include two inner loops.

It can be also found that the unbalance fault reduces the system nonlinearity and stretches the axis trajectory along the Y direction by comparing the trajectories under misalignment (C) and unbalance-misalignment (F), single crack (D) and unbalance-single crack (G), multiple cracks (E) and unbalance-multiple cracks (H). From the trajectories with unbalance-single crack (G) and unbalance-multiple cracks (H), unbalance-misalignment-single crack (K) and unbalance-misalignment-multiple cracks (L), the multi-crack rotor has larger trajectories and stronger nonlinearity than the single crack rotor. This is because the interaction between multiple cracks increases the flexibility and alters the nonlinearity of stiffness of the rotor system [55]. In the cases of coupled faults, Figs. 6(B) and (F), (D) and (I), (E) and (J), (G) and (K), (H) and (L) show that the misalignment fault only has a slight effect on the trajectories of the cracked rotor. Therefore, the shape change of axis trajectories cannot reflect the diverse fault conditions of the rotor system.

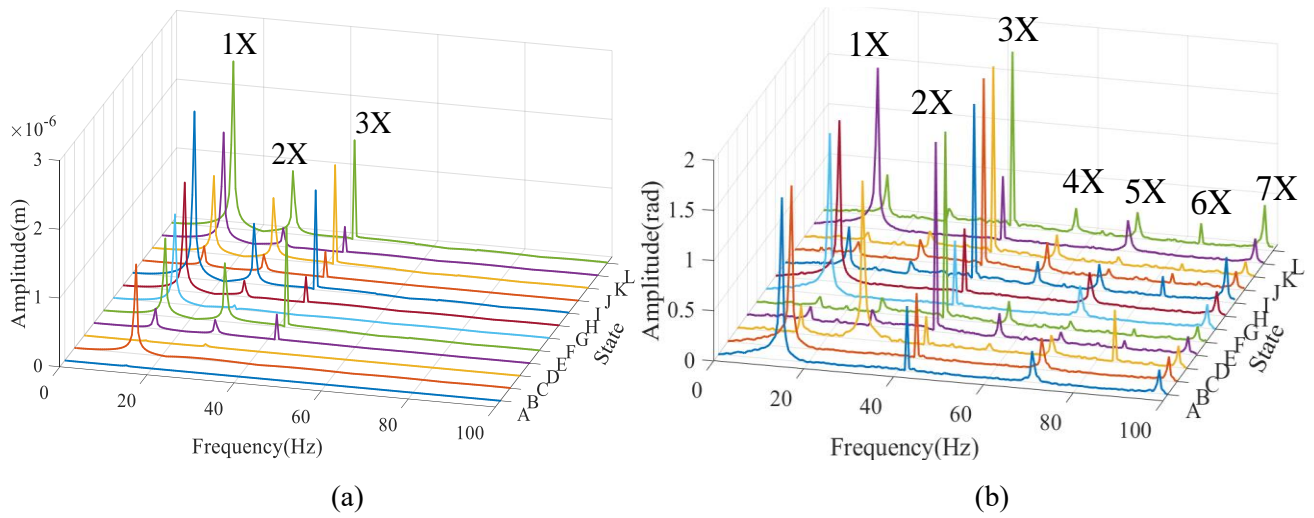


Fig. 7. Frequency spectra with different rotor states in noise-free environment, (a) Displacement signals in Y direction, (b) Trajectory phase angles.

Fig. 7 is the frequency spectra of the trajectory phase angles and the vibration displacement signals in Y direction obtaining through Fourier transform. It can be seen from Fig. 7(a) that there is no obvious harmonic information in the spectra of displacement signal under the states of healthy (A) and misalignment (C) since the magnitudes of the harmonic components are much smaller than those of other rotor faults. The unbalance fault (B) only arouses a 1X component, coinciding with the results in Ref. [42] and [44]. The unbalance-misalignment fault (F) induces a significant 1X and a slight 2X component, while the remaining eight faults have excited 1X, 2X and 3X components of different magnitudes.

It is evident from Fig. 7(b) that the spectra of trajectory phase angles show richer harmonic

components compared to Fig. 7(a), which will be beneficial to represent the dynamic properties of the rotor system under different kinds of faults. The spectra contain 3X, 5X, 7X components and a dominant 1X under the states of healthy (A), unbalance (B), unbalance-misalignment (F), unbalance-single crack (G) and unbalance-misalignment-single crack (K). In addition, the 3X component is dominant in the conditions of single crack (D), multiple cracks (E), misalignment-single crack (I) and misalignment-multiple cracks (J). The spectra contain 1X-7X components under the faults of unbalance-multiple cracks (H) and unbalance-misalignment-multiple cracks (L). It can be observed that the magnitudes of 2X and 6X components induced by misalignment (C) are more significant than those of other faults, which can be used as the features of the misalignment fault.

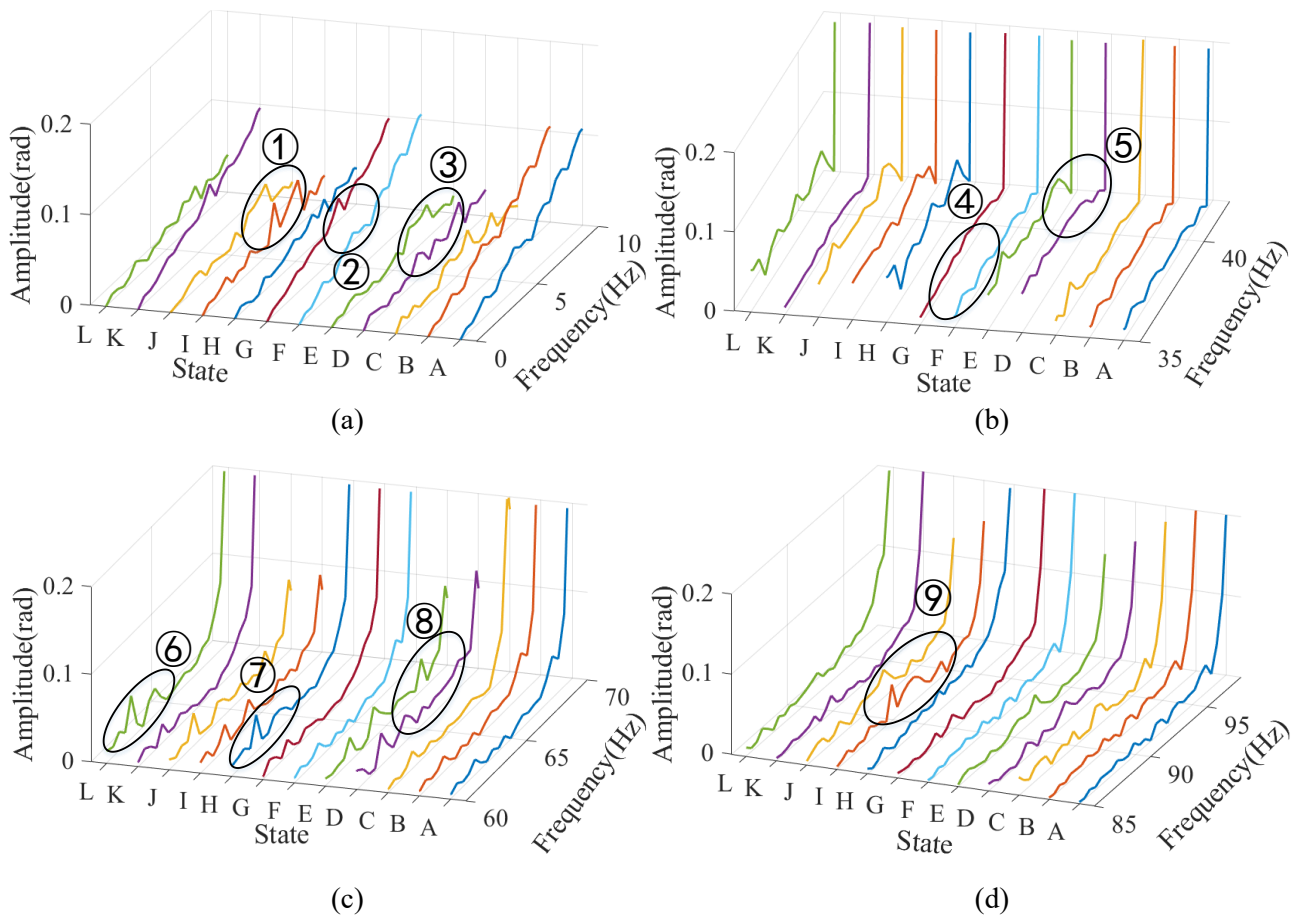


Fig. 8. Partial enlargement of frequency spectra of trajectory phase angles with different rotor states in noise-free environment, (a) 0-10 Hz, (b) 35-42 Hz, (c) 60-70 Hz, (d) 85-98 Hz.

There are many other harmonic components with smaller amplitudes in the spectra of trajectory phase angles besides the 1X-7X components, which also provide valuable discriminative information for different faults. Fig. 8 shows the spectra of trajectory phase angles in the frequency bands of 0-10 Hz, 35-42 Hz, 60-70 Hz and 85-98 Hz, in which the obvious differences are marked by nine black rings. The twelve states of the rotor system can be classified into nine categories based on the harmonic information of trajectory phase feature, depicted in Fig. 9, compared to the five categorizations through the axis trajectory plots (shown in Table 2). Therefore, the extracted trajectory phase feature has significant superiority in characterizing the dynamic properties of the rotor system with different states. However,

although the spectra of trajectory phase angles can provide more harmonic details, it is still difficult to classify the twelve rotor states fully, since some harmonic components containing valuable discrepancy information have relatively small magnitudes.

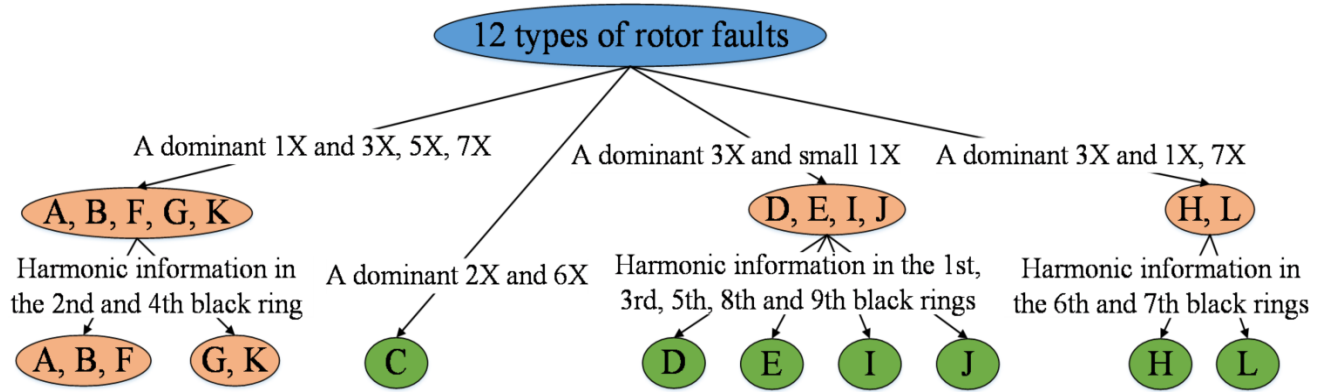


Fig. 9. Classification results of twelve rotor states based on trajectory phase feature.

3.2 Classification results without noise

To fully exploit the distinguishing information of different kinds of faults contained in the trajectory phase feature, a LightGBM model is introduced to classify the twelve states of the rotor system based on the extract trajectory phase feature. Some of hyper-parameters of the LightGBM model are chosen to ensure the classification accuracy, listed in Table 3, and the others are default values.

Table 3. Hyper-parameters of LightGBM model.

Parameter	Value	Parameter	Value
Objective	Multiclass	Learning_rate	0.01
N_estimators	200	Max depth	30
Num_class	12	Num_leaves	200

The extracted trajectory phase angles under the twelve rotor states in a noise-free environment are fed into the LightGBM model. Data in each kind of fault contains 6000 samples, of which 70% are randomly selected as training set for the model training, and the remaining 30% are used as testing set to evaluate the model performance. To illustrate the universality of the trajectory phase feature, the same samples are imported into the XGBoost [56] and GBDT [57] models. The hyper-parameter N_estimators for the two models are 15 and 150 respectively, and other hyper-parameters are same as LightGBM or the default values. The classification results of the three models for different rotor states are listed in Table 4. And the corresponding confusion matrices are shown in Fig. 10, where the horizontal axis represents the predicted rotor states and the vertical axis denotes the actual ones. The values on main diagonal of confusion matrix indicate the recognition accuracy of each kind of fault, while others are the misdiagnosis rate of the relevant faults.

Table 4. Classification results of three machine learning models for twelve rotor states.

Model	Accuracy (%)												Time (s)	
	A	B	C	D	E	F	G	H	I	J	K	L		Mean
LightGBM	100	96.3	100	98.9	95.2	93.8	100	100	100	98.9	100	100	98.6	170
XGBoost	100	100	100	96.6	92.9	100	100	98.6	99.0	96.6	100	100	98.6	200
GBDT	100	100	100	100	88.0	100	100	100	100	91.0	100	100	98.2	730

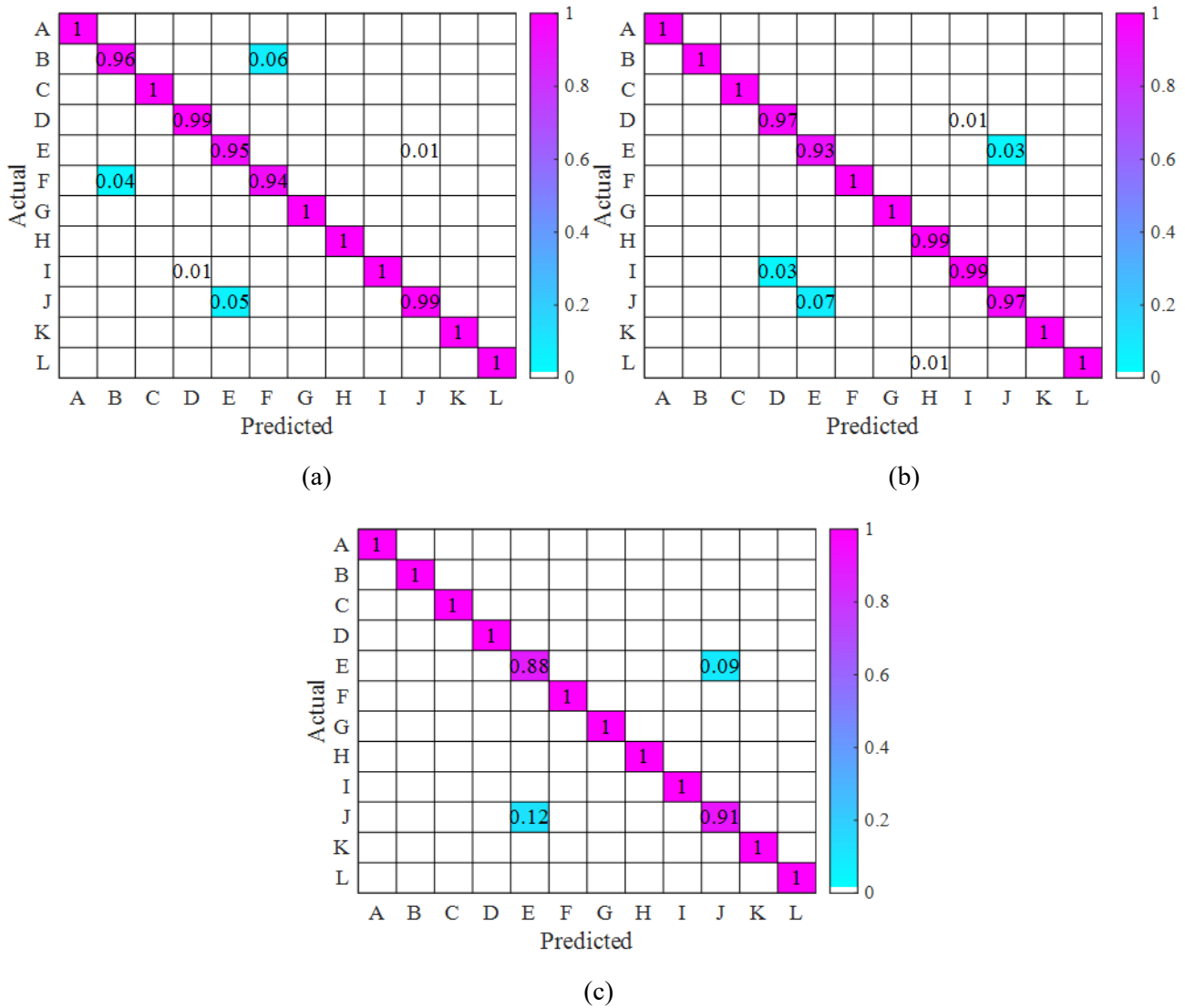


Fig. 10. Confusion matrices of three machine learning models, (a) LightGBM, (b) XGBoost, (c) GBDT.

It can be seen from Table 4 and Fig. 10 that both LightGBM and XGBoost models can accurately identify seven rotor states, and the minimum recognition rates for any fault are 93.8% (unbalance-misalignment) and 92.9% (multiple cracks), respectively. The GBDT model can accurately classify ten rotor states with a lowest identification rate of 88.0% for the multiple cracks fault. The foregoing three models have all achieved a mean classification accuracy over 98.0% for the twelve rotor states, in which the LightGBM model has faster fitting speed and lower time consumption. It is worth noting that the average recognition accuracy of the three models is less than 10.0% by taking the

vibration displacement signals with the twelve states as the input samples directly. Therefore, the extracted trajectory phase feature has a good applicability and can excellently realize the multi-fault classification of rotor systems.

3.3 Classification results with noise

In practice, the raw vibration displacement signals of a rotor system are vulnerable to noise contamination, which will cause intricate and distorted axis trajectories, eventually resulting in poor recognition accuracy and incorrect diagnosis results. The parameter-optimized VMD method is introduced to decompose and denoise the trajectory phase angles under different SNRs (20, 15, 10, 5, 0, -5, -10, -15, -20 dB) for the multi-fault classification of the rotor system in noisy environments.

The axis trajectory and trajectory phase angle under the coupled fault of unbalance-misalignment-multiple cracks at SNR = -20 dB are shown in Fig. 11. It can be observed from Fig. 11(a) that the noisy axis trajectory has become messy. And the extracted trajectory phase angle in Fig. 11(b) also becomes miscellaneous, and the harmonic components are almost completely masked by noise.

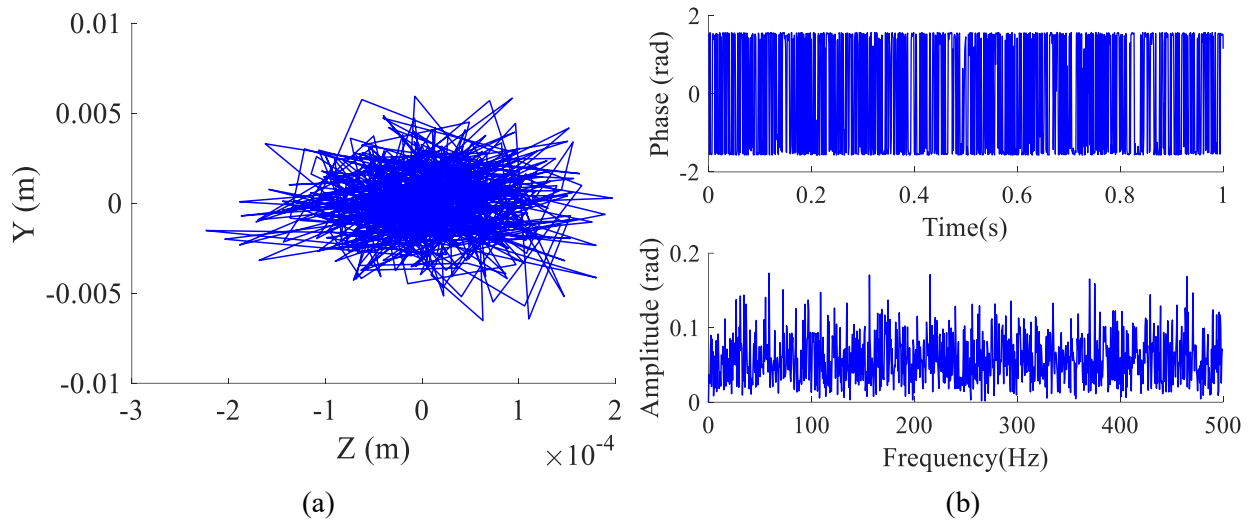


Fig. 11. Vibration responses under unbalance-misalignment-multiple cracks at SNR = -20 dB, (a) Axis trajectory, (b) Trajectory phase angle.

Then the parameter-optimized VMD method (with $K = 11$ and $\alpha = 2730$) is applied to decompose and denoise the trajectory phase angle, and a group of IMFs can be obtained, displayed in Fig. 12. The first two IMFs (whose center frequencies are equal to the fundamental and natural frequency of the rotor system, respectively), and other ones with the sample entropy satisfying Eq. (10) are selected to reconstruct the trajectory phase angle shown in Fig. 13.

$$\frac{\text{SampEn}(\text{IMF}_k)}{\max\{\text{SampEn}(\text{IMF}_k)\}} < \eta \quad (10)$$

where $\max\{\text{SampEn}(\text{IMF}_k)\}$ denotes the maximum sample entropy, η is set as 0.5.

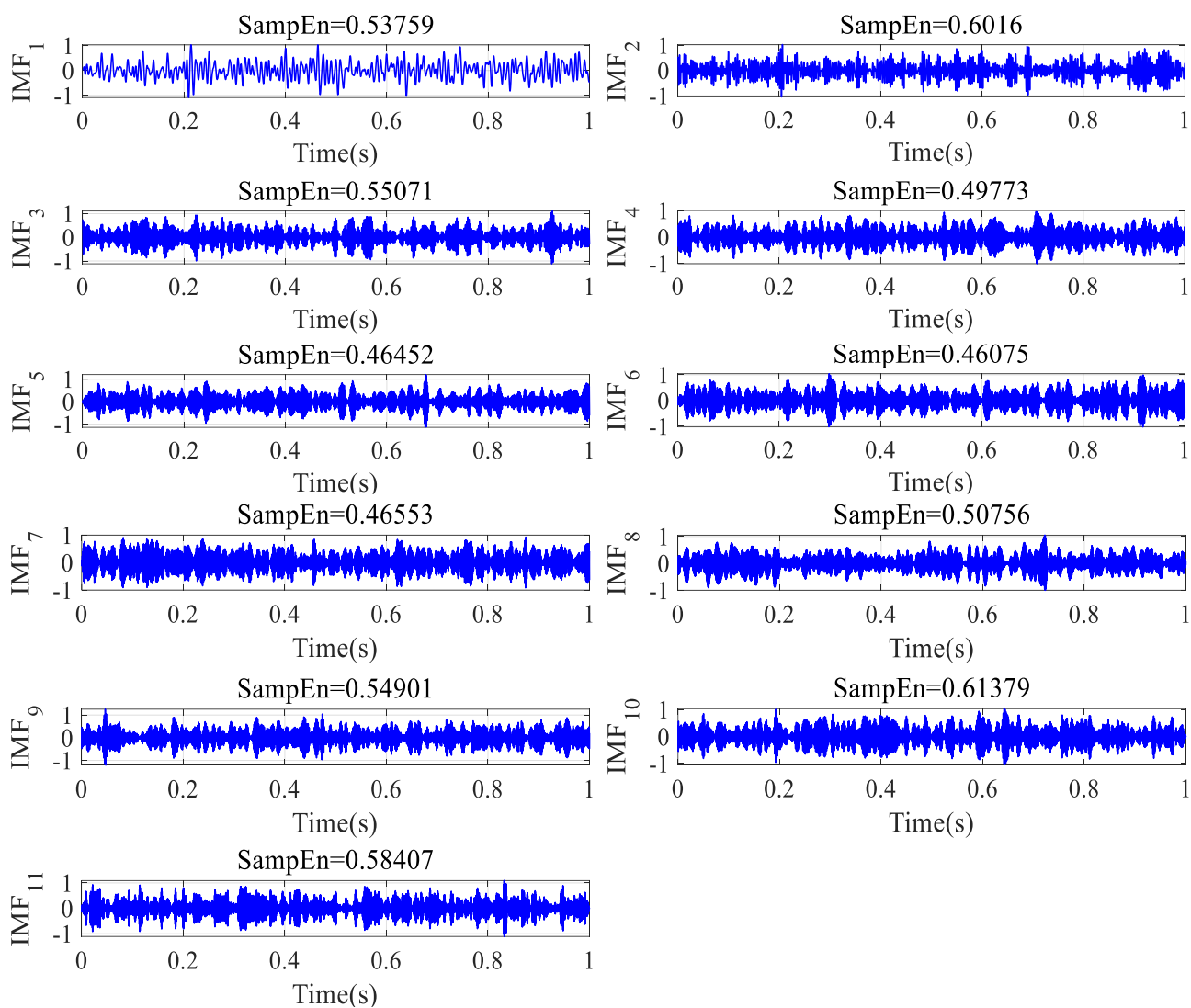


Fig. 12. Decomposition result of parameter-optimized VMD.

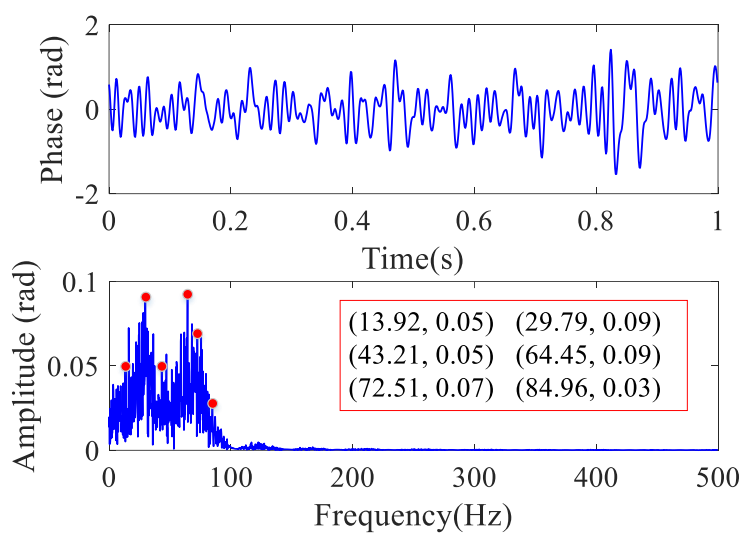


Fig. 13. Denoised reconstructed trajectory phase angle.

As can be seen from Figs. 11(b) and 13 that the denoised reconstructed phase angle has filtered out most of the Gaussian white noise, although there are still some residual noise components. Meanwhile, the valuable information relating to rotor motion is also highlighted. The first six frequency components associated with the system vibration are marked with red dots in Fig. 13 and their coordinate values are displayed in the red box.

After noise reduction, the reconstructed trajectory phase angles under the twelve states are imported into the LightGBM model for the multi-fault classification of the rotor system at different SNRs. And the classification results are given in Table 5 and mapped to accuracy diagram in Fig. 14.

Table 5. Classification results of twelve rotor states at different SNRs.

SNR (dB)	Accuracy (%)												Mean
	A	B	C	D	E	F	G	H	I	J	K	L	
20	100	100	100	92.2	100	100	100	100	89.8	100	100	100	98.5
15	88.7	100	100	100	100	97.2	100	100	100	98.9	100	97.7	98.5
10	96.3	90.8	100	94.7	100	100	100	96.1	88.3	96.6	100	100	96.9
5	100	100	100	93.0	91.3	96.7	97.6	100	100	82.3	100	100	96.7
0	100	98.8	100	97.7	88.8	100	100	95.1	87.2	91.6	100	97.1	96.4
-5	90.5	98.8	100	97.5	98.8	90.7	98.5	100	95.7	95.5	100	90.4	96.3
-10	94.3	97.8	92.8	93.7	92.8	96.4	97.3	95.5	96.8	100	96.3	96.5	95.9
-15	100	96.0	97.6	98.9	100	95.8	100	98.7	97.6	96.1	79.4	83.5	95.3
-20	98.5	98.8	98.9	98.4	97.8	97.0	90.1	96.6	100	92.8	79.5	80.2	94.1

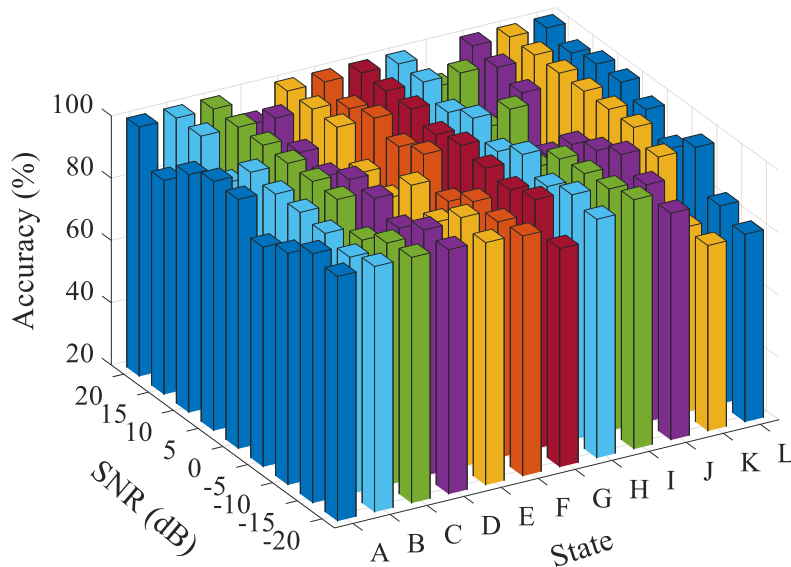


Fig. 14. Classification accuracy diagram of twelve rotor states at different SNRs.

It can be observed from Table 5 and Fig. 14 that the average recognition accuracy of the LightGBM model for the twelve rotor states decreases gradually with the increase of SNR, while the minimum average recognition accuracy has exceeded 94.0%. When the SNRs are -15 dB and -20 dB, the classification accuracy for the first ten faults is greater than 92.5%, and that for the unbalance-

misalignment-single crack (K) and unbalance-misalignment-multiple cracks (L) faults is about 80.0%. Therefore, the proposed method can enable effective multi-fault classification of the rotor system at different SNRs. And the extracted trajectory phase feature has excellent robustness to noise, even in strong noisy environments.

4. Experimental Verification

In this section, the vibration experiments with twelve rotor states of different kinds (including healthy, unbalance, misalignment, single crack, multiple cracks, unbalance-misalignment, unbalance-single crack, unbalance-multiple cracks, misalignment-single crack, misalignment-multiple cracks, unbalance-misalignment-single crack, unbalance-misalignment-multiple cracks) are performed to validate the feasibility and applicability of the proposed method. The rotation speed of the shaft is $1/3\Omega_0'$ (Ω_0' is the first critical speed of the experimental bench, 2562 rpm). The sampling frequency is 5000 Hz, two measuring points are located at the first disc and in the middle of rotating shaft.

4.1 Experimental setup

The test bench mainly contains six parts: two ball bearings, two discs, four eddy current displacement sensors, three rotating shafts (healthy, single crack, multiple cracks), a flexible coupling and a servo motor, shown in Fig. 15. Table 6 gives the parameters of each component. The length of each rotating shaft is 0.6 m and the diameter is 0.01 m. The breathing crack on shaft is slit by wire cutting with a depth of 0.002 m. The unbalance fault is generated by adjusting the eccentric bolts mounted on two shaft discs. The misalignment fault is obtained by a spacer with a thickness of 0.001 m installed under the first bearing seat. Two sensors at identical measuring point have a relative angle of $\pi/2$ rad to collect the vibration displacement signals in the Y and Z directions.

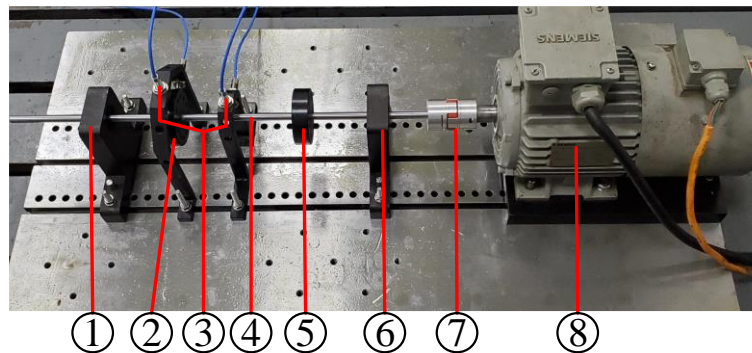


Fig. 15. Illustration of rotor test bench, ① Bearing 1, ② Disc 1, ③ Eddy current displacement sensors, ④ Shaft, ⑤ Disc 2, ⑥ Bearing 2, ⑦ Flexible coupling, ⑧ Servo motor.

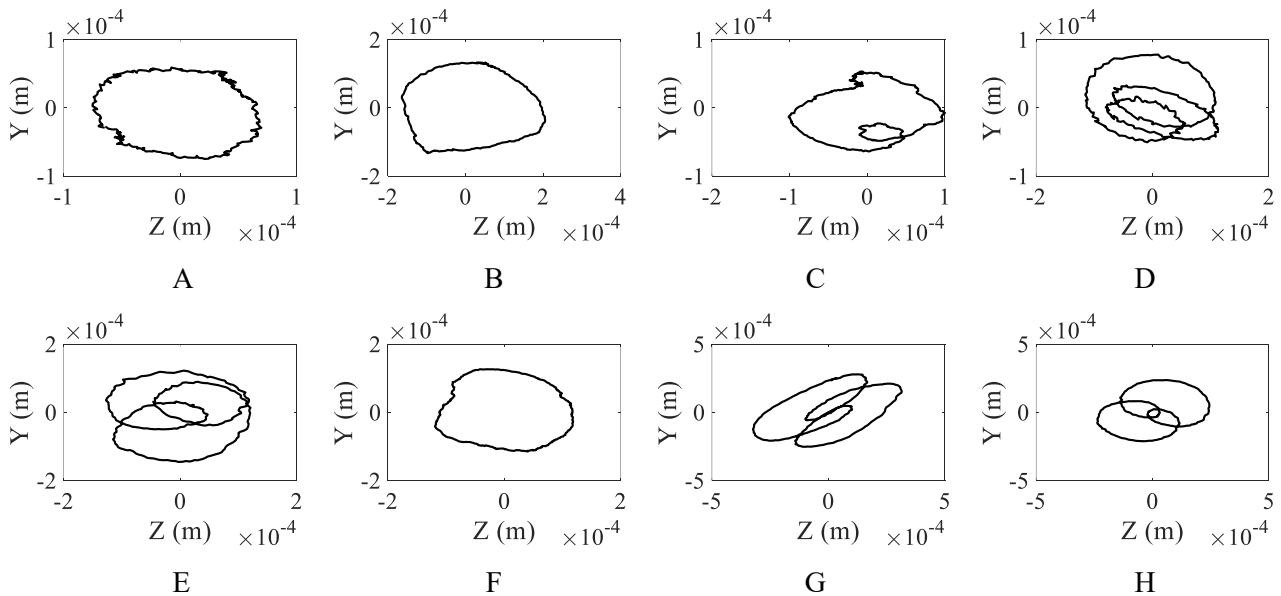
Table 6. Parameters of test bench.

Part	Type	Quantity
Bearing	SKF-6300	2
Disc	45# steel	2
Shaft	40Cr	3
Flexible coupling	LM-45-10-24	1
Servo motor	SIEMENSE G90A IP55	1
Eddy current displacement sensor	ZA21-0803	4
Motor control system	VFD-M 1.5 kW	1
Signal acquisition system	DHDAS5922N	1

4.2 Data Description

Fig. 16 shows the experimental axis trajectories under the twelve rotor states, which has similar shapes to the simulated ones. Coinciding with the simulated axis trajectories in Figs. 6(A)-(B) and (F), the experimental ones under the states of healthy, unbalance, and unbalance-misalignment have the similar trajectory shape of a ring. The simulated and experimental trajectories under the misalignment fault both contain an inner loop, shown in Figs. 6(C) and 16(C). The experimental axis trajectories with a single crack, multiple cracks, unbalance-multiple cracks, misalignment-single crack, misalignment-multiple cracks, unbalance-misalignment-multiple cracks all include two inner loops, same as the simulated ones in Fig. 6.

As can be seen from Figs. 16(G) and (K) that the experimental trajectories under unbalance-single crack and unbalance-misalignment-single crack have an or two inner loops, while the simulated ones contain two concaves shown in Figs. 6(G) and (K). The reason is that the depth of the single crack obtained by wire cutting is greater than 0.002 m (the actual depth is 0.0023 m), leading to the increase in nonlinearity of stiffness of the rotor system. Additionally, the test noise and the rotation speed fluctuation of the servo motor causes some undesirable small disturbances in the experimental trajectories.



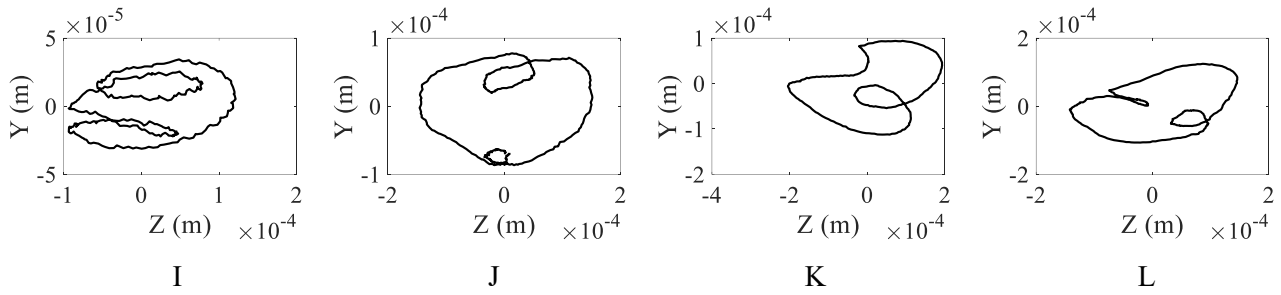


Fig. 16. Experimental axis trajectories with different rotor states, A: healthy, B: unbalance, C: misalignment, D: single crack, E: multiple cracks, F: unbalance-misalignment, G: unbalance-single crack, H: unbalance-multiple cracks, I: misalignment-single crack, J: misalignment-multiple cracks, K: unbalance-misalignment-single crack, L: unbalance-misalignment-multiple cracks.

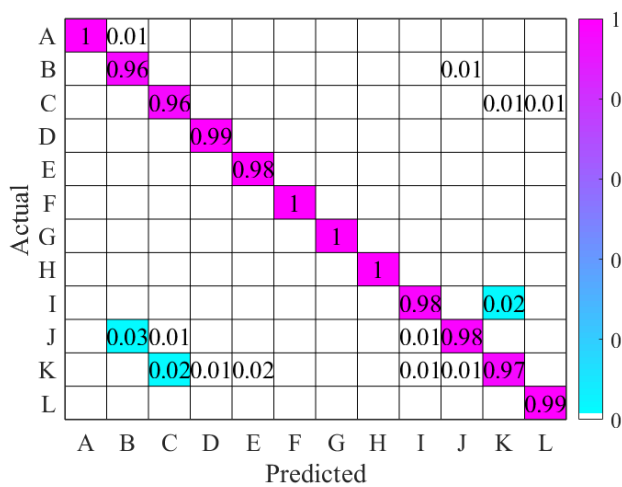
4.3 Experimental results and discussions

To verify the generalization ability of the proposed method, the trajectory phase angles extracted from the experimental axis trajectories are input into the LightGBM, XGBoost and GBDT models. The classification results of the twelve rotor states are given in Table 7, and the confusion matrices are displayed in Fig. 17.

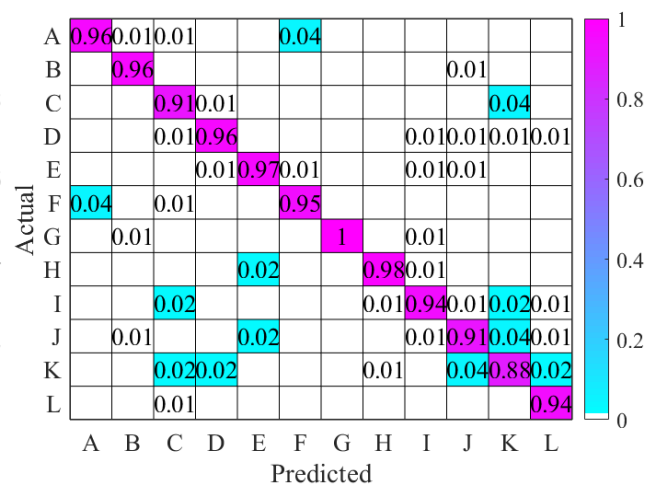
It can be observed that the average classification accuracy of the three models has exceeded 94.5% for the twelve states, and the minimum identification accuracy is about 90.0% for any fault. Consequently, the proposed method has a good adaptability to experimental data, despite there are more misdiagnosis cases than the simulated results.

Table 7. Experimental classification results of three machine learning models for twelve rotor states.

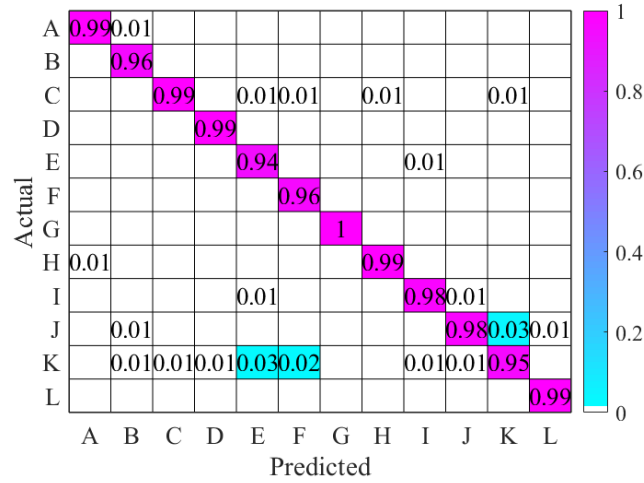
Model	Accuracy (%)												Mean
	A	B	C	D	E	F	G	H	I	J	K	L	
LightGBM	100	95.8	96.4	99.0	98.4	100	100	100	97.7	97.7	96.6	98.7	98.4
XGBoost	96.4	95.8	90.7	95.7	96.8	95.1	100	97.6	94.2	91.1	88.0	93.8	94.6
GBDT	98.8	95.8	98.8	99.0	94.0	96.4	100	98.8	97.7	97.7	95.4	98.7	97.6



(a)



(b)



(c)

Fig. 17. Confusion matrices of three models for experimental data, (a) LightGBM, (b) XGBoost, (c) GBDT.

The trajectory phase angles extracted from the experimental axis trajectories at different SNRs (20, 15, 10, 5, 0, -5, -10, -15, -20 dB) are fed into the LightGBM model after noise attenuation. The multi-fault classification results are shown in Table 8, and the accuracy diagram is displayed in Fig. 18.

It can be found from Table 8 and Fig. 18 that the mean classification accuracy under different SNRs exceeds 93.0% and the recognition rate of any kind of fault is over 77.5%. And there is a minimum recognition rate around 78.0% for the misalignment (C) and single crack (D) faults as SNR = -15 dB and -20 dB, respectively. Hence, based upon the experimental trajectory phase feature, the proposed method can classify different rotor states in different noisy environments, coinciding with the simulated results in Table 5 and Fig. 14.

Table 8. Experimental classification results of twelve rotor states at different SNRs.

SNR (dB)	Accuracy (%)												Mean
	A	B	C	D	E	F	G	H	I	J	K	L	
20	100	98.9	97.5	95.5	98.8	96.7	98.9	100	97.0	98.7	95.2	98.8	98.0
15	97.8	97.5	96.7	98.9	98.7	94.9	100	100	97.5	93.3	95.7	95.6	97.2
10	95.6	94.8	100	100	97.0	97.8	98.9	97.9	97.5	97.0	94.7	93.9	97.1
5	95.8	96.3	96.8	96.6	98.7	96.0	100	97.3	94.3	98.5	97.8	90.4	96.5
0	96.2	92.0	97.4	92.9	97.4	93.3	98.8	96.4	96.3	100	94.8	98.8	96.2
-5	97.6	95.2	93.6	94.0	92.3	93.8	98.6	96.3	96.3	97.6	98.8	94.9	95.8
-10	100	98.8	95.1	96.6	98.6	93.5	85.4	100	91.2	90.6	95.6	92.9	94.9
-15	83.9	98.7	78.9	96.6	91.3	92.8	97.7	98.9	96.8	98.8	96.3	97.2	94.0
-20	97.3	81.6	98.8	77.7	91.8	96.0	95.2	96.4	98.8	97.2	97.9	89.7	93.2

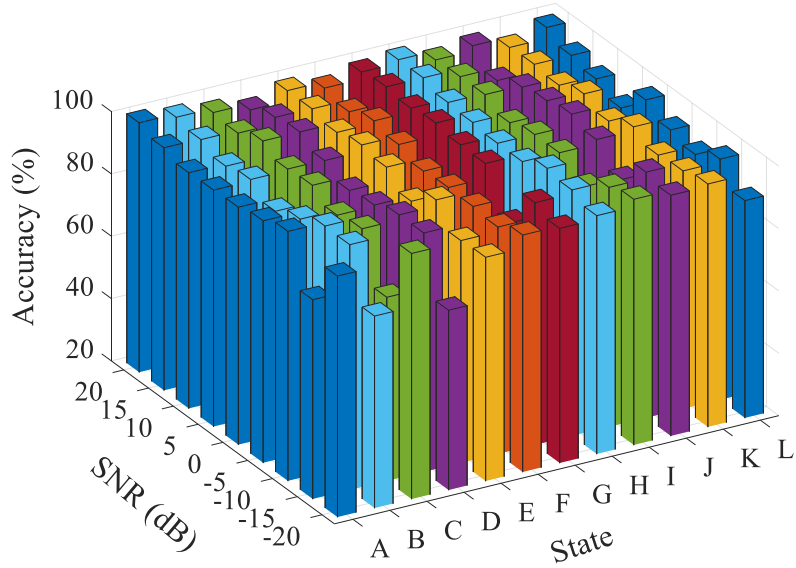


Fig. 18. Experimental classification accuracy diagram of twelve rotor states at different SNRs.

To verify the correctness of the proposed method, the experimental classification accuracy of healthy state (A), misalignment (C), single crack (D) and misalignment-single crack (I) is compared with that in Ref. [58] as SNR = 10 dB, 0 and -10 dB. The relevant results are listed in Table 9.

It can be found from Table 9 that the mean classification accuracy of the proposed method achieves 96.6%, greater than 95.9% with the method in Ref. [58], especially the classification accuracy maintains a high value (95.7%) in a strong noise environment when SNR is -10 dB, which verifies the good robustness to noise of the proposed method in multi-fault classification of rotor systems.

Table 9. Comparison of classification accuracy at different SNRs.

SNR (dB)	Classification accuracy (%)	
	Method in Ref. [58]	Proposed method
10	100	98.3
0	100	95.7
-10	87.67	95.7
Mean	95.9	96.6

5. Conclusions

As it is difficult to distinguish multiple rotor faults with similar dynamics phenomena in noisy environments, a multi-fault classification method is proposed by combining the phase feature of axis trajectory, a parameter-optimized VMD method and a LightGBM model. The trajectory phase feature is extracted from an axis trajectory to characterize the rotor motion under healthy, three single faults and eight coupled faults by integrating the frequency, amplitude and phase information in axis trajectory. A parameter-optimized VMD method based on NSGA-III is applied to decompose and denoise the trajectory phase angles at different SNRs (20, 15, 10, 5, 0, -5, -10, -15, -20 dB). And the LightGBM model is introduced for the multi-fault classification of rotor systems. Simulations and experiments are

performed to verify the proposed method. The specific conclusions are presented below.

(1) The Fourier spectra of trajectory phase angles contain many harmonic components including the 1X-7X components and other components with smaller amplitudes, which can provide sufficient discrepancy information for the multi-fault classification of rotor systems.

(2) The twelve rotor states can be classified into nine categories based on the phase feature of axis trajectory.

(3) The proposed method can classify multiple faults of rotor systems in different noisy environments. The average classification accuracy of the twelve states exceeds 93.0%, and the recognition rate for any fault is greater than 77.5%.

The method in this work can enable effective multi-fault classification of rotor systems in noisy environments, which is promising for the condition monitoring and fault diagnosis of rotating machine in engineering. However, this research only focuses on the rotor system at 1/3 subcritical speed, without considering the influence of speed change, which will be the priority of future work.

Declaration of conflicting interests

The authors declare that there is no conflict of interest.

Funding

This work was supported by the National Natural Science Foundation of China [No. 51875482] and the Natural Science Foundation of Sichuan Province of China [No. 2022NSFSC0416].

References

- [1] Y. Lei, B. Yang, X. Jiang, F. Jia, N. Li, A.K. Nandi, Applications of machine learning to machine fault diagnosis: A review and roadmap, *Mech Syst Signal Pr*, 138 (2020) 106587.
- [2] A.C. Altunışık, F.Y. Okur, S. Karaca, V. Kahya, Vibration-based damage detection in beam structures with multiple cracks: modal curvature vs. modal flexibility methods, *Nondestruct Test Eva*, (2018) 1-21.
- [3] E. Carden, Vibration based condition monitoring: A review, *Struct Health Monit*, 3 (2004) 355-377.
- [4] W. Fan, P. Qiao, Vibration-based damage identification methods: A review and comparative study, *Struct Health Monit*, 9 (2010).
- [5] J. Xie, J. Chen, Y. Peng, Y. Zi, A new concept of instantaneous whirling speed for cracked rotor's axis orbit, *Applied Sciences*, 9 (19) (2019).
- [6] L. Xiang, Y. Zhang, A. Hu, Crack characteristic analysis of multi-fault rotor system based on whirl orbits, *Nonlinear Dynam*, 95 (4) (2019) 2675-2690.
- [7] N. Bachschmid, P. Pennacchi, A. Vania, Diagnostic significance of orbit shape analysis and its application to improve machine fault detection, *J Braz Soc Mech Sci*, XXVI (2004).
- [8] M. Torkhani, L. May, P. Voinis, Light, medium and heavy partial rubs during speed transients of rotating machines: Numerical simulation and experimental observation, *Mech Syst Signal Pr*, 29 (2012) 45-66.
- [9] W. Li, L. Ji, W. Shi, Y. Wang, L. Zhou, X. Jiang, M. Thomas, Vibration of shaft system in the mixed-flow pump induced by the rotor-stator interaction under partial load conditions, *Shock Vib*, 2018 (2018) 2059784.

- [10] W. Li, L. Ji, W. Shi, Y. Yang, M. Awais, Y. Wang, X. Xu, Correlation research of rotor-stator interaction and shafting vibration in a mixed-flow pump, *Journal of Low Frequency Noise, Vibration and Active Control*, 39 (1) (2019) 72-83.
- [11] P. Pennacchi, A. Vania, Diagnosis and model based identification of a coupling misalignment, *Shock Vib*, 12 (2005) 607319.
- [12] C. Fu, K. Lu, Y. Yang, Z. Xie, A. Ming, Nonlinear vibrations of an uncertain dual-rotor rolling bearings system with coupling misalignment, *J Nonlinear Math Phy*, 29 (2) (2022) 388-402.
- [13] Y. Liu, Y. Zhao, J. Li, H. Lu, H. Ma, Feature extraction method based on NOFRFs and its application in faulty rotor system with slight misalignment, *Nonlinear Dynam*, 99 (2) (2020) 1763-1777.
- [14] C. Guo, J. Yan, W. Yang, Crack detection for a Jeffcott rotor with a transverse crack: An experimental investigation, *Mech Syst Signal Pr*, 83 (2017) 260-271.
- [15] L. Xiong, C. Hua, L. Lv, D. Dong, H. Ouyang, A model-based dynamic characteristics analysis of a coupled multi-crack rotor system, *Nonlinear Dynam*, 110 (3) (2022) 2197-2223.
- [16] Y. Yang, J. Wang, Y. Wang, C. Fu, Q. Zheng, K. Lu, Dynamical analysis of hollow-shaft dual-rotor system with circular cracks, *Journal of Low Frequency Noise, Vibration and Active Control*, 40 (3) (2020) 1227-1240.
- [17] H. Khorrami, S. Rakheja, R. Sedaghati, Vibration behavior of a two-crack shaft in a rotor disc-bearing system, *Mech Mach Theory*, 113 (2017) 67-84.
- [18] X. Ma, H. Ma, H. Qin, X. Guo, C. Zhao, M. Yu, Nonlinear vibration response characteristics of a dual-rotor-bearing system with squeeze film damper, *Chinese J Aeronaut*, 34 (10) (2021) 128-147.
- [19] M. Shi, Y. Yang, W. Deng, J. Wang, C. Fu, Analysis of dynamic characteristics of small-scale and low-stiffness ring squeeze film damper-rotor system, *Applied Sciences*, 12 (14) (2022).
- [20] P. Varney, I. Green, Nonlinear phenomena, bifurcations, and routes to chaos in an asymmetrically supported rotor - stator contact system, *J Sound Vib*, 336 (2015) 207-226.
- [21] J. Lin, Y. Zhao, P. Wang, Y. Wang, Q. Han, H. Ma, S. Elias, Nonlinear responses of a rotor-bearing-seal system with pedestal looseness, *Shock Vib*, 2021 (2021) 9937700.
- [22] R. Gasch, Dynamic behaviour of the Laval rotor with a transverse crack, *Mech Syst Signal Pr*, 22 (4) (2008) 790-804.
- [23] Y. Li, Z. Luo, J. Wang, H. Ma, D. Yang, Numerical and experimental analysis of the effect of eccentric phase difference in a rotor-bearing system with bolted-disk joint, *Nonlinear Dynam*, 105 (3) (2021) 2105-2132.
- [24] Y. Li, Z. Luo, J. Liu, H. Ma, D. Yang, Dynamic modeling and stability analysis of a rotor-bearing system with bolted-disk joint, *Mech Syst Signal Pr*, 158 (2021) 107778.
- [25] H. Ma, C. Shi, Q. Han, B. Wen, Fixed-point rubbing fault characteristic analysis of a rotor system based on contact theory, *Mech Syst Signal Pr*, 38 (1) (2013) 137-153.
- [26] H. Ma, H. Li, X. Zhao, H. Niu, B. Wen, Effects of eccentric phase difference between two discs on oil-film instability in a rotor - bearing system, *Mech Syst Signal Pr*, 41 (1) (2013) 526-545.
- [27] H. Ma, H. Li, H. Niu, R. Song, B. Wen, Nonlinear dynamic analysis of a rotor-bearing-seal system under two loading conditions, *J Sound Vib*, 332 (23) (2013) 6128-6154.
- [28] J. Zhou, H. Wu, W. Wang, K. Yang, Y. Hu, X. Guo, C. Song, Online unbalance compensation of a maglev rotor with two active magnetic bearings based on the LMS algorithm and the influence coefficient method, *Mech Syst Signal Pr*, 166 (2022) 108460.
- [29] M.A. Ahad, N. Iqbal, S.M. Ahmad, M. Khan, Detailed modelling and LQG/LTR control of a 2-DOF radial active magnetic bearing for rigid rotor, *J Braz Soc Mech Sci*, 43 (5) (2021) 234.

- [30] K. Kalista, J. Liska, J. Jakl, A vibration sensor-based method for generating the precise rotor orbit shape with general notch filter method for new rotor seal design testing and diagnostics, *Sensors-Basel*, 21 (15) (2021).
- [31] S. Lahriiri, H.I. Weber, I.F. Santos, H. Hartmann, Rotor-stator contact dynamics using a non-ideal drive—Theoretical and experimental aspects, *J Sound Vib*, 331 (20) (2012) 4518-4536.
- [32] X. Zhao, T.H. Patel, M.J. Zuo, Multivariate EMD and full spectrum based condition monitoring for rotating machinery, *Mech Syst Signal Pr*, 27 (2012) 712-728.
- [33] X. Zhang, Y. Yang, H. Ma, M. Shi, P. Wang, A novel diagnosis indicator for rub-impact of rotor system via energy method, *Mech Syst Signal Pr*, 185 (2023).
- [34] X. Zhang, Y. Yang, M. Shi, Y. Zhang, P. Wang, An energy track method for early-stage rub-impact fault investigation of rotor system, *J Sound Vib*, 516 (2022) 116545.
- [35] L. Qu, J. Lin, Y. Liao, M. Zhao, Changes in rotor response characteristics based diagnostic method and its application to identification of misalignment, *Measurement*, 138 (2019) 91-105.
- [36] X. Zhang, Y. Yang, M. Shi, A. Ming, P. Wang, Novel energy identification method for shallow cracked rotor system, *Mech Syst Signal Pr*, 186 (2023) 109886.
- [37] J. Sinha, Higher order spectra for crack and misalignment identification in the shaft of a rotating machine, *Struct Health Monit*, 6 (2007) 325-334.
- [38] Z. Li, W. Li, X. Zhao, Feature frequency extraction based on singular value decomposition and its application on rotor faults diagnosis, *J Vib Control*, 25 (6) (2019) 1246-1262.
- [39] M.J. Guo, W.G. Li, Q.J. Yang, X.Z. Zhao, Y.L. Tang, Amplitude filtering characteristics of singular value decomposition and its application to fault diagnosis of rotating machinery, *Measurement*, 154 (2020).
- [40] T. Liu, M. Lyu, Z. Wang, S. Yan, An identification method of orbit responses rooting in vibration analysis of rotor during touchdowns of active magnetic bearings, *J Sound Vib*, 414 (2018) 174-191.
- [41] W. Yang, P.J. Tavner, Empirical mode decomposition, an adaptive approach for interpreting shaft vibratory signals of large rotating machinery, *J Sound Vib*, 321 (3) (2009) 1144-1170.
- [42] H. Wu, J. Zhou, C. Xie, J. Zhang, Y. Huang, Two-dimensional time series sample entropy algorithm: Applications to rotor axis orbit feature identification, *Mech Syst Signal Pr*, 147 (2021) 107123.
- [43] L. Qu, X. Liu, G. Peyronne, Y. Chen, The holospectrum: A new method for rotor surveillance and diagnosis, *Mech Syst Signal Pr*, 3 (3) (1989) 255-267.
- [44] P. Goldman, A. Muszynska, Application of full spectrum to rotating machinery diagnostics, *Orbit-Abingdon*, 20 (1) (1999) 17-21.
- [45] D. K., Z. D., Variational mode decomposition, *Ieee T Signal Proces*, 62 (3) (2014) 531-544.
- [46] X. Zhang, Q. Miao, H. Zhang, L. Wang, A parameter-adaptive VMD method based on grasshopper optimization algorithm to analyze vibration signals from rotating machinery, *Mech Syst Signal Pr*, 108 (2018) 58-72.
- [47] Y. Zhao, C. Li, W. Fu, J. Liu, T. Yu, H. Chen, A modified variational mode decomposition method based on envelope nesting and multi-criteria evaluation, *J Sound Vib*, 468 (2020) 115099.
- [48] K. Deb, R.B. Agrawal, An evolutionary many-objective optimization algorithm using reference-point-based nondominated sorting approach, part I: Solving problems with box constraints, *Ieee T Evolut Comput*, 18 (4) (2014) 577-601.
- [49] Z.N. Haji, S.O. Oyadiji, An evolutionary many-objective optimization algorithm using reference-point based nondominated sorting approach, part II: Handling constraints and extending to an adaptive approach, *Ieee T Evolut Comput*, 18 (4) (2014) 602-622.
- [50] A. Delgado-Bonal, A. Marshak, Approximate entropy and sample entropy: A comprehensive tutorial, *Entropy-Switz*,

21 (2019) 541.

- [51] D. Wang, C. Hua, D. Dong, B. He, Z. Lu, Crack parameters identification based on a Kriging surrogate model for operating rotors, *Shock Vib*, 2018 (2018) 1-12.
- [52] G. Ke, Q. Meng, T. Finley, T. Wang, W. Chen, W. Ma, Q. Ye, T. Liu, LightGBM: A highly efficient gradient boosting decision tree, *Neural information processing systems foundation*, 2017, pp. 3147-3155.
- [53] M. Tang, Q. Zhao, S.X. Ding, H. Wu, L. Li, W. Long, B. Huang, An improved LightGBM algorithm for online fault detection of wind turbine gearboxes, *Energies*, 13 (4) (2020).
- [54] Q. Fang, B. Shen, J. Xue, A new elite opposite sparrow search algorithm-based optimized LightGBM approach for fault diagnosis, *J Amb Intel Hum Comp*, (2022).
- [55] L. Xiong, C. Hua, F. Yang, D. Dong, H. Ouyang, Dynamic characteristics analysis of a coupled multi-crack rotor system, *Journal of Physics: Conference Series*, 2184 (1) (2022) 12040.
- [56] T. Chen, C. Guestrin, XGBoost: A scalable tree boosting system, *Association for Computing Machinery*, 2016, pp. 785-794.
- [57] J.H. Friedman, Greedy function approximation: A gradient boosting machine, *Ann Stat*, 29 (5) (2001) 1189-1232.
- [58] W. Zhao, C. Hua, D. Dong, H. Ouyang, A novel method for identifying crack and shaft misalignment faults in rotor systems under noisy environments based on CNN, *Sensors-Basel*, 19 (23) (2019) 5158.